

Arctic soil patterns analogous to fluid instabilities

Rachel C. Glade^a, Michael Fratkin^a, Mehdi Pouragha^b,
Ali Seiphoori^c, and Joel Rowland^a

January 21, 2021

a) EES-14, Los Alamos National Lab, Los Alamos, NM, 87545. b) Department of Civil and Environmental Engineering, Carleton University, 1125 Colonel By Drive, Ottawa, ON, K1S 5B6. c) Department of Earth, Atmospheric and Planetary Sciences, Massachusetts Institute of Technology, Green Bldg, The, 77 Massachusetts Ave, Cambridge, MA 02139

This manuscript is a non-peer reviewed preprint that has been submitted to EarthArXiv. The paper has been submitted to PNAS for peer review. Updated versions will be uploaded as the paper (hopefully) traverses the peer review process.

Arctic soil patterns analogous to fluid instabilities

Rachel Glade^{a,1}, Michael Fratkin^a, Mehdi Pouragha^b, Ali Seiphoori^c, and Joel Rowland^a

^aEES-14, Los Alamos National Lab, Los Alamos, NM, 87545. ; ^bDepartment of Civil and Environmental Engineering, Carleton University, 1125 Colonel By Drive, Ottawa, ON, K1S 5B6; ^cDepartment of Earth, Atmospheric and Planetary Sciences, Massachusetts Institute of Technology, Green Bldg, The, 77 Massachusetts Ave, Cambridge, MA 02139

This manuscript was compiled on January 21, 2021

Slow-moving arctic soils commonly organize into striking large-scale spatial patterns called solifluction terraces and lobes. Though these features impact hillslope stability, carbon storage and release, and landscape response to climate change, no mechanistic explanation exists for their formation. Everyday fluids—such as paint dripping down walls—produce markedly similar fingering patterns resulting from competition between viscous and cohesive forces. Here we use a scaling analysis to show that soil cohesion and hydrostatic effects can lead to similar large-scale patterns in arctic soils. A large new dataset of high-resolution solifluction lobe spacing and morphology across Norway supports theoretical predictions and indicates a newly observed climatic control on solifluction dynamics and patterns. Our findings provide a quantitative explanation of a common pattern on Earth and other planets, illuminating the importance of cohesive forces in landscape dynamics. These patterns operate at length and time scales previously unrecognized, with implications toward understanding fluid-solid dynamics in particulate systems with complex rheology.

solifluction | fluid instabilities | climate | granular fingering | periglacial

Periodically frozen soil—a temporally evolving mixture of granular material, fluid, and ice—is one of the most complex natural materials found on planetary surfaces. While its rheology is not well understood, arctic soil deformation commonly produces large, distinctive meters-to-tens of meters-scale spatial patterns visible in aerial images (Figure 1A). Patterns are organized in both the downslope and cross-slope directions. Regular downslope-oriented terraces of soil are characterized by raised fronts that protrude 1-2 meters above the surrounding topography (Figure 1A,C). Terrace fronts are commonly broken into finger-like lobes evenly spaced cross-slope (Figure 1A,B). Known as solifluction features, these patterns form due to a combination of frost heave, in which segregation ice growth lofts soil upwards, and gelifluction, a slow flow-like relaxation of partially saturated soil once it thaws in the summer (1, 2). While a rich history of experimental and global field observations over the past century have characterized solifluction processes and velocities ($\sim 10^{-1} - 10^1$ cm/year) (2, 3), there exists no agreed-upon rheological model for solifluction that can offer quantitative and qualitative explanations for the striking patterns it produces. Renewed interest in these features primarily stems from a need to predict Arctic landscape response to climate change and storage and release of permafrost carbon, as well as to predict and mitigate arctic slope instabilities due to thawing permafrost (4).

Strikingly similar patterns develop in simple fluids, where competition between viscous and cohesive forces drives a suite of common instabilities in thin films. For example, the evenly spaced fluid fingers that form when painting a wall, icing a cake, or sloshing oil in a frying pan are known as “contact line instabilities” at fluid fronts (7, 11) (Figure 1A). Only recently

have soft solids (12) and granular materials (13–18) been shown to exhibit patterns and morphology that resemble those of thin-film fluids. Notably, (13) found that small cohesive forces between sand grains produce an effective surface tension relevant at macroscopic length scales, causing a steady stream of sand to break into droplets similar to a Rayleigh-Plateau instability. However, connections between fluid and granular instabilities—especially regarding the role of cohesion—remain a frontier in materials science.

Here we take the first step toward utilizing quantitative connections with fluid and granular mechanics to better understand solifluction processes and patterns. We present a conceptual model of solifluction pattern formation in which solifluction lobes (resembling fluid fingers) arise as a cross-slope instability on the fronts of terraces (resembling fluid roll waves) formed during an initial downslope instability (Figure 1A,B). While we present data for both instabilities, we focus mainly on the cross-slope patterns. First, we discuss how key ingredients that control fluid contact line instabilities—viscosity, velocity, fluid thickness, and surface tension—may translate to soil. By adopting an analogy between fluid and soil dynamics, we suggest a formal scaling analysis relating solifluction wavelengths to active soil thickness, topographic slope, and cohesion-drive effects at the soil front. Using high-resolution topographic data from over 3000 solifluction lobes across 25 sites in Norway, we show that scaling between solifluction wavelengths and slope, lobe height, and lobe front angle generally agrees with our theoretical analysis. Data from these sites show that lobe morphology is strongly correlated with elevation, which likely represents a climate control on solifluction processes due to the dependence of frost heave on mean annual daily temperature

Significance Statement

Slow-moving arctic soils form patterns resembling those found in common fluids, such as paint and cake icing drips. Inspired by fluid instabilities, we develop a new conceptual model for soil patterns and use mathematical analysis to predict their wavelength. In particular, we propose that soil patterns arise due to competition between gravity and cohesion, or the “stickiness” of soil grains. We compare our theoretical predictions with a new data set of soil features from Norway, finding that soil patterns are controlled by both fluid-like properties as well as climate. Our work provides the first physical explanation for a common pattern on both Earth and Mars, with implications for our understanding of landscapes and complex materials composed of both granular and fluid components.

R.C.G., M.F., and J.R. designed research; M.F. and R.C.G. analyzed data; all authors contributed to development of theory and writing of paper

The authors declare no competing interests.

¹To whom correspondence should be addressed. E-mail: rcglade@lanl.gov

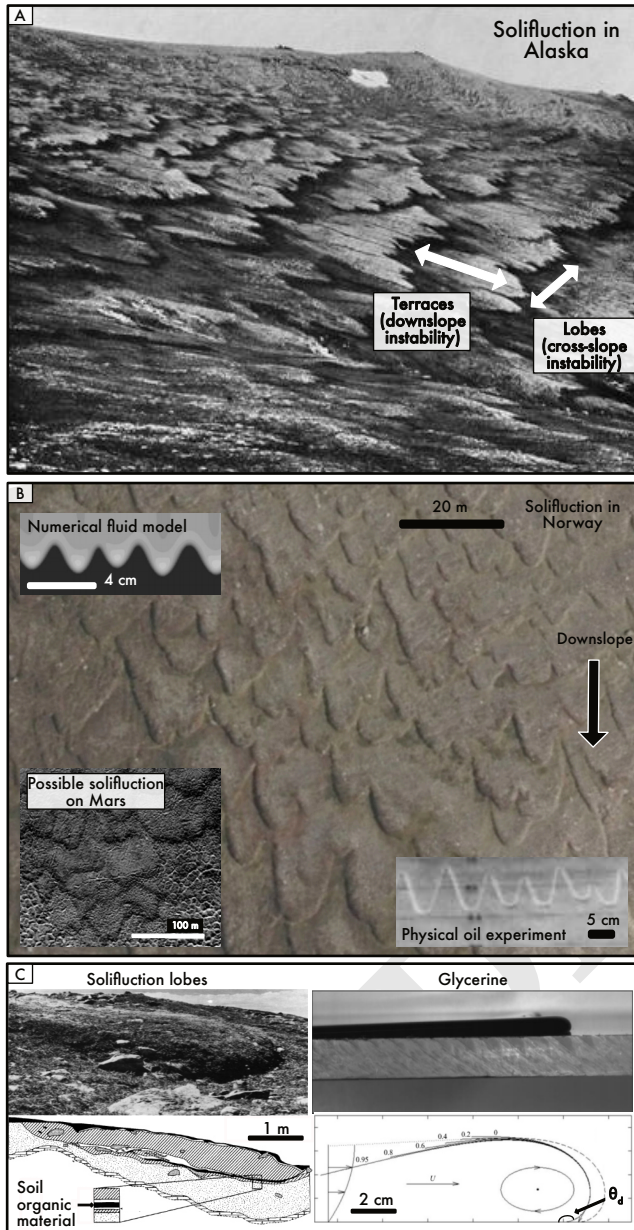


Fig. 1. A) Solifluction terraces and lobes in Chicken Creek, Alaska. Photo by Philip S. Smith. B) Examples of solifluction and fluid patterns. Background: Orthophoto of solifluction lobes in Norway, copyright Kartverket. Upper left: Numerical model image reprinted from (5). Lower left: Possible solifluction on Mars, reprinted from (6). Lower right: Photo of front of oil flowing down plane, reprinted from (7). C) Morphology and dynamics of solifluction lobes vs. surface tension-dominated flows. Upper left: Solifluction lobe in Colorado, reprinted from (8). Lower left: Map of trenched lobe, with soil organic layer showing rollover motion. Adapted from (9). Upper right: Gravity driven glycerine front. Lower right: schematic of glycerine front showing rollover motion. Shape of nose derived from Young-Laplace equation for surface tension effects. Numbers indicate profile evolution through time, and dashed line illustrates profile at next moment in time. Dynamic contact angle θ_d is shown. Both reprinted from (10).

amplitude (T_a) and mean annual air temperature (MAAT). We discuss how cohesion not only slows down soil motion but results in a state change in soil behavior, with implications for Arctic landscape response to climate change and interpretation of past climates on Earth and other planets. Our work shows that even in creeping granular-fluid-ice materials, competition between driving stress and cohesion can result in large-scale patterns similar to those found in fluids, with implications for our understanding of the rheological behavior of complex materials.

Fluid Fingering Instabilities

First, we briefly describe fingering instabilities in fluid films. The qualitative explanation for contact line instabilities is simple: at a fluid interface in a thin film, cohesive forces in the form of surface tension hold back the flow, allowing the front to thicken into a capillary ridge. With a slight initial perturbation, competition between body forces, which cause thicker zones to move faster, and surface tension, which induces transverse flow under bumps, drives the growth of fingers with a regular wavelength. Experiments (e.g., (7, 19, 20)), linear stability analysis (e.g. (11, 21)), and numerical models (e.g. (5, 22)) have determined that the wavelength of fluid contact line instabilities is given by

$$\lambda = BH \left(\frac{3\sigma}{v\mu} \right)^{1/3} \quad [1]$$

where H is the fluid thickness, B is a dimensionless constant (14 for Newtonian fluids, 35 for shear thinning yield stress fluids (19), μ is the fluid dynamic viscosity, v is a characteristic velocity, σ is the surface tension, and $\sigma/v\mu$ is the inverse capillary number Ca . This means that flows with greater thickness or surface tension produce larger wavelengths, while more viscous or faster moving flows produce smaller wavelengths. Note that v depends on both μ and H ; therefore, for a laminar Newtonian fluid in which average velocity $v = \rho g H \sin \theta / \mu$, Eqn. 1 becomes $\lambda = BH^{2/3} \left(\frac{3\sigma}{\rho g \sin \theta} \right)^{1/3}$. Ca has also been shown to control the dynamic contact angle θ_d at the fluid front (Figure 1C) according to the Voinov-Tanner-Cox law, such that $\theta_d^2 \sim Ca^m$, where $m = 1$ for a Newtonian fluid (23), $m > 1$ for a viscoelastic fluid (24) and $m < 1$ for shear thinning fluids (25). The positive relationship between θ_d and Ca shows that the steeper the contact angle, the faster/more viscous the flow (or the lower the cohesion/surface tension). This provides a link between finger morphology and dynamics, and because both wavelength and contact angle depend on Ca , we would expect a negative power law trend between the two of the form $\frac{\lambda}{H} \sim \theta_d^{1/m}$.

Solifluction Lobes as Fluid-like Instabilities

We argue that the solifluction phenomenon qualitatively exhibits all the necessary ingredients for a fluid-like instability. Here we describe how each ingredient may translate to soil, resulting in a new conceptual model of solifluction pattern formation (Figure 2C).

Contact line instabilities initiate at a raised fluid front. For solifluction, we propose that a downslope instability forms evenly spaced solifluction terraces that operate similarly to a fluid front. With raised fronts $\sim 1 - 2m$ tall and wavelengths much larger than soil thickness ($\sim 10^1 - 10^2m$) (Figure 1A; 3E), this downslope instability features prominently in the

121 landscape. Though the cause of the downslope instability is
122 unclear, we argue it is likely a result of soil rheology, similar
123 to non-inertial waves recently observed in shear thickening
124 fluids or fluids with resisting forces at the free surface (26)
125 (see Discussion). With enough heterogeneity in topography,
126 soil properties (such as moisture, cohesion, and grain size), or
127 vegetation, smooth terrace fronts may break into solifluction
128 lobes evenly spaced cross-slope (Figure 1A,B) with wavelengths
129 on the order of $1 - 10^2$ m. Although the thickness, h , of these
130 features is large relevant to fluid thin films, ~ 1 m, the hillslope-
131 wide lateral length scale of motion, l , supports the idea that
132 they may behave like thin films ($h \ll l$) (27).

133 While solifluction rheology and mechanistic relationships
134 between velocity and depth are still unclear, data and mod-
135 els show that velocity likely increases with total active soil
136 thickness due to freeze-thaw processes (2, 28). Field mea-
137 surements across the globe have found solifluction velocities
138 ranging from $10^{-1} - 10^1$ cm/yr (2). Considering the soil as
139 a slow-moving fluid, these slow velocities suggest very high
140 viscosities. We compile every available field-measured and
141 experimental vertical velocity profile from the literature and
142 find that most exhibit an exponential decrease in velocity with
143 depth (Figure 2A) while a few studies exhibit more complex
144 profiles (SI Appendix, Fig S2). We then calculate effective
145 viscosity μ_{eff} as the ratio between shear stress τ and strain
146 rate du/dz : $\tau = \mu_{eff} \frac{du}{dz}$. We find large μ_{eff} ranging from
147 $10^5 - 10^{12}$ Pa-s. In contrast to a Newtonian fluid with con-
148 stant viscosity, velocity profiles show that effective viscosity
149 increases with depth (Figure 2B), indicating a non-Newtonian-
150 like flow behavior. While a proper description of solifluction
151 rheology should explicitly take into account granular physics,
152 our first order assumption of non-Newtonian fluid-like behav-
153 ior is likely acceptable for a wet granular material (e.g., (29))
154 (see Discussion).

155 Surface tension at the front is the last key ingredient for a
156 contact line instability. While recent studies have shown that
157 intergranular cohesion can produce an effective surface tension
158 in granular materials at small length scales (e.g. (13)), this
159 concept is not physically relevant for ~ 1 m thick soils where
160 overburden pressure vastly outweighs any possible pressure
161 due to surface tension. However, we argue that increased
162 cohesion and decreased soil velocities at solifluction fronts
163 allow soil buildup and transverse flow due to hydrostatic pres-
164 sure, akin to the behavior of surface tension-dominated fluids.
165 There are many sources of cohesion that can lend substantial
166 strength to soils, including microbes (e.g., (30)), permafrost,
167 vegetation (e.g., (31)), capillary bridges due to moisture con-
168 tent (e.g., (32)), clay composition, and solid bridging due to
169 polydispersity ((33)). We propose that increased drainage at
170 the open boundary at the front of a solifluction terrace or lobe
171 likely increases the effectiveness of many of these cohesion
172 sources. First, drainage at the front may decrease ice lens
173 formation and subsequent frost heave and soil transport. Ice
174 lenses require the presence of adequate moisture and specific
175 temperature conditions in order to form (e.g., (34)) that may
176 be easily disrupted at an open boundary. This would result
177 in a decrease in soil velocities at the front of the lobe. Sec-
178 ond, drainage and consolidation at the front may increase
179 the strength of capillary bridges, which can increase capillary
180 suction and the resulting apparent cohesion (35, 36). Finally,
181 moisture conditions at the front may encourage vegetation

182 growth there, lending added cohesion in turf-banked lobes
183 ((37, 38)). While soil moisture patterns in solifluction lobes
184 are complex (37) and cohesion patterns have never been mea-
185 sured, available field evidence supports the idea of a stalled
186 lobe front. Displacement markers in the field show soil buildup
187 behind solifluction lobe fronts and transverse flow toward the
188 middle/front of lobes, akin to behavior in fluid fingers (8).
189 Solifluction lobe morphology (thickened front and steep, some-
190 times overhanging contact angle) (e.g., (8)) and dynamics
191 (tractor tread-style rollover motion at the front) (8, 9, 39)
192 resemble those of surface-tension dominated flows (Figure 1C).
193 Additionally, commonly documented retrograde motion uphill
194 in solifluction lobes points toward strong effects of cohesion
195 (2, 40), likely resulting from temporally evolving strength of
196 capillary bridges.

197 Conceptual Model

198 We propose that the solifluction lobe instability is initiated
199 and controlled by competition between these elements: 1)
200 the body force due to gravity, which moves thicker material
201 downhill faster 2) cohesion at the front, which resists flow, and
202 3) lateral flow due to hydrostatic pressure under topographic
203 bumps (Figure 2B), with cross-slope wavelengths set by these
204 competing processes (Figure 2B). This is similar to fluid con-
205 tact line fingering in that competition between a body force
206 and resisting force due to cohesion at the front initiates and
207 controls the preferred wavelength of the instability, where in-
208 creased cohesion at the front takes the place of surface tension.
209 Finally, while formulations of fluid contact line instabilities
210 ignore hydrostatic effects because surface tension dominates,
211 here we include hydrostatic pressure that drives lateral flow
212 in the presence of inevitable topographic roughness in natural
213 landscapes.

214 We develop our analysis to be as general as possible, with-
215 out assuming a specific source of cohesion at the front of
216 the lobe. While vegetation has been shown to be important
217 for solifluction patterns (38), the existence of non-vegetated
218 lobes precludes vegetation as a necessary ingredient for their
219 formation. Here we focus on solifluction lobes without large
220 boulders; however, stone-banked lobes exhibit grain size segre-
221 gation with large boulders at the front and sides of the lobe (8).
222 This likely leads to a similar effect in which boulder jamming
223 at the front of the lobe stalls flow. Thus our general conceptual
224 model should apply to both turf-banked and stone-banked
225 lobes on Earth and Mars, as well as unvegetated lobes with
226 relatively homogeneous grain sizes as are observed on Mars
227 (41).

228 Wavelength scaling analysis

229 Inspired by fluid theory for contact line instabilities, we take
230 the first step toward deriving an expression for solifluction lobe
231 wavelengths. Because solifluction rheology is uncertain, our
232 analysis avoids assumptions of Newtonian flow. In contrast to
233 instabilities in surface-tension dominated fluids, we allow for
234 hydrostatic effects given the likelihood of natural topographic
235 roughness in the field. We examine laminar flow down a plane,
236 accounting for hydrostatic pressure in both the downslope (x)
237 and cross-slope (y) directions. Cohesion has been shown to
238 control effective viscosity in granular materials (e.g., (29, 42)).
239 Therefore, to account for cohesion at solifluction fronts, we

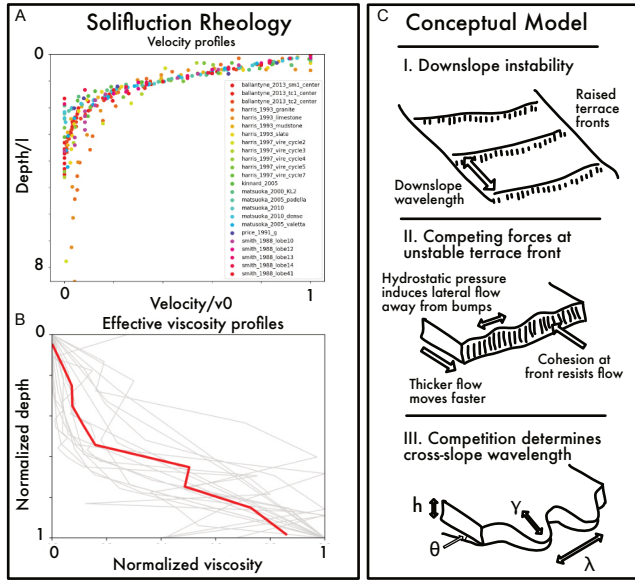


Fig. 2. A) Vertical velocity profiles compiled from the literature, observed both in the field and laboratory experiments. See non-normalized plots in SI Appendix Figure S3. B) Vertical viscosity profiles computed from velocity profile show general increase in effective viscosity with depth. See non-normalized plots in SI Appendix Figure S4. C) Conceptual model of solifluction lobe pattern formation.

where h_0 is a characteristic height, μ_0 is a characteristic viscosity, γ is a characteristic length scale in the x direction that describes a distance over which the viscosity varies, and λ is a characteristic length scale in the y direction (Figure 2C). Retaining only the dimensional leading coefficients and simplifying:

$$\frac{2 \sin \theta}{\gamma} - \frac{h_0}{\gamma^2} + \frac{h_0}{\lambda^2} = 0 \quad [5]$$

We note that the viscosity cancels out, and its only effect lies in γ . We are mainly interested in λ , which we assume to be the cross-slope wavelength between solifluction lobes. Assuming the body force (first term) dominates over the hydrostatic pressure gradient (second term), we find:

$$\lambda \sim \sqrt{\frac{h_0 \gamma}{2 \sin \theta}} \quad [6]$$

This suggests that the cross-slope wavelength increases with soil thickness and the characteristic length over which viscosity changes due to dynamics at the front, and decreases with basal slope (which we assume to be equivalent to x directed topographic slope averaged over a distance \gg length of a lobe). Though the particular scaling differs from that for fluids in Eqn. 1, our relationship is similar in that cross-slope wavelength is projected to exhibit a power law increase with height and cohesion and a decrease with topographic slope. These fundamental similarities between solifluction lobe and fluid finger wavelengths also suggest that while we do not yet have a prediction for the contact angle at the front of lobes, we might expect an inverse relationship between cross-slope wavelength normalized by height and the contact angle as described above for fluids.

Solifluction patterns in Norway

To explore these ideas in real landscapes, we collected high resolution morphologic and topographic data from 26 highly-patterned solifluction sites across Norway (Figure 3). We manually measured 3000 individual lobes from submeter LiDAR-derived digital elevation models (DEMs) (freely available at [Hoydedata](#)) to obtain cross-slope lobe wavelength, height, lobe length, and lobe front/riser angle (hereafter referred to as contact angle), terrace (downslope) wavelength, and topographic slope (see Methods). We find that cross-slope wavelengths range from 2-100 m, with a mean of 13m. This range agrees with previous studies (41), and values are generally smaller but overlap with those found on Mars (Figure 3B). Trends between lobe morphology metrics and topography agree with theoretical predictions. Cross-slope wavelength increases with lobe height/topographic slope, as expected from our scaling analysis (Eqn. 6). Though the data include a large amount of scatter, binned average wavelengths show that our theoretical prediction describes the general trend well (Figure 3C). Note that in order to better explain the data we would need constraints on γ , which may also depend on lobe height and explain the jelly bean shape of the data. A better understanding of rheology could also be incorporated in our analysis to improve predictions. Our theory predicts only scaling rather than absolute wavelengths; however, the empirically best fit power law coefficient (≈ 8) suggests that cross-slope wavelength $\lambda \approx 6 \sqrt{h_0 \gamma / \sin \theta}$.

allow effective viscosity to vary in the (x) direction. Here we present the simplest approach to scaling; see SI Appendix Section I for alternative approaches that produce similar results.

For a laminar fluid flowing down an inclined plane, under hydrostatic conditions upstream from the front, the basal shear stress is:

$$\tau_0 = -\rho g h \sin \theta + \rho g h \frac{\partial h}{\partial x} \quad [2]$$

where ρ is the bulk density, g is gravity, h is the fluid depth, and θ is the underlying slope. To avoid assumptions of Newtonian rheology, but without assuming a particular form of a power-law fluid, we define a bulk viscosity μ such that $\tau_0 = -\mu U/h$, where U is the vertically averaged velocity in the x (downhill) direction. To account for cohesion at the front, we allow viscosity to change in the x direction. Solving for the downslope velocity and assuming that cross-slope velocity arises only from the hydrostatic pressure gradient, we can solve the continuity equation at steady-state and retain only first-order terms (see methods) to find:

$$\frac{3 \sin \theta}{\mu} \frac{\partial h}{\partial x} - \frac{h \sin \theta}{\mu^2} \frac{\partial \mu}{\partial x} - \frac{h}{\mu} \frac{\partial^2 h}{\partial x^2} + \frac{h}{\mu} \frac{\partial^2 h}{\partial y^2} = 0 \quad [3]$$

where the first two terms represent the body force, the third term is the downslope hydrostatic component (x direction), and the fourth term is the cross-slope hydrostatic component (y direction). Now we can scale terms by dimensionless quantities (indicated with hats) as follows:

$$\begin{aligned} h &= h_0 \hat{h} \\ \mu &= \mu_0 \hat{\mu} \\ x &= \gamma \hat{x} \\ y &= \lambda \hat{y} \end{aligned} \quad [4]$$

320 As expected from theory, we see a negative power law trend
 321 between wavelength/height and contact angle. This observa-
 322 tion is consistent with theory for dynamic contact angle of
 323 a droplet rolling down a flat substrate. However, to prop-
 324 erly predict the relationship between cross-slope wavelength
 325 and contact angle, we would need theory equivalent to the
 326 Voinov-Tanner-Cox law that accounts for cohesion rather than
 327 surface tension. We also find that lobe aspect ratio (L/W)
 328 slightly increases with topographic slope, as observed in fluid
 329 experiments (SI Appendix, Fig S5) (43). Most lobes are wider
 330 than they are long, exhibiting a sawtooth shape similar to
 331 that observed for fluids on gently sloping planes (SI Appendix,
 332 Fig. S5) (Figure 1B). Finally, we observe a positive relation-
 333 ship between downslope terrace wavelength and lobe height
 334 averaged by site (Figure 3E), but no clear relationship with
 335 topographic slope is discerned (SI Appendix, Fig S6). While
 336 we currently lack a prediction for the scaling of downslope
 337 wavelength, our data provide the first step toward developing
 338 a better understanding of the phenomenon (see Discussion).

339 Large amounts of scatter in the field data likely contain
 340 interesting information about lithology, vegetation, climate,
 341 and other unknown parameters that differ between sites. How-
 342 ever, that average wavelength trends agree with our theory
 343 inspired by simple fluids is remarkable and supports the idea
 344 that solifluction patterns operate similarly to fluid contact line
 345 instabilities.

346 Climate controls

347 Our data show a meaningful increase in solifluction lobe height
 348 and cross-slope wavelengths with elevation (Figure 4), point-
 349 ing toward a climate control on lobe morphology and pattern
 350 formation due to the lapse rate, or change in temperature
 351 with height in the atmosphere. Though solifluction features
 352 are traditionally thought to be climate-controlled and have
 353 often been used to interpret past climate, limited data exist
 354 for co-located climate metrics and solifluction lobe morphology
 355 and dynamics (44). However, recent work on frost cracking
 356 in rock (45–47) illuminates the climatic conditions required
 357 for segregation ice growth and frost heave, the main drivers of
 358 solifluction (2, 48). (46) find that the depth and intensity of
 359 frost cracking increases with annual temperature amplitude
 360 and decreases with MAAT. To explore this idea, we compare
 361 high temporal resolution climate metrics from extensive mon-
 362 itoring stations in Norway over the last 20 years (49) with
 363 solifluction lobe morphology for each site shown in Figure 3A.
 364 Consistent with frost cracking predictions, we find an increase
 365 in finger wavelength and lobe height with annual temperature
 366 amplitude, corresponding with a general decrease in MAAT
 367 (Figure 4). Other differences between high and low elevations
 368 may explain observed morphology trends. While we do not
 369 see strong relationships with mean annual snowfall, precipita-
 370 tion, or time spent in the frost cracking window (SI Appendix,
 371 Figs 7-9), shortwave radiation or vegetation coverage may be
 372 important. We interpret the data to show that climate primar-
 373 ily affects the depth of solifluction processes, which in turns
 374 affects the wavelengths. This is supported by a much weaker
 375 relationship between elevation and wavelength normalized by
 376 height (SI Appendix, Fig 10).

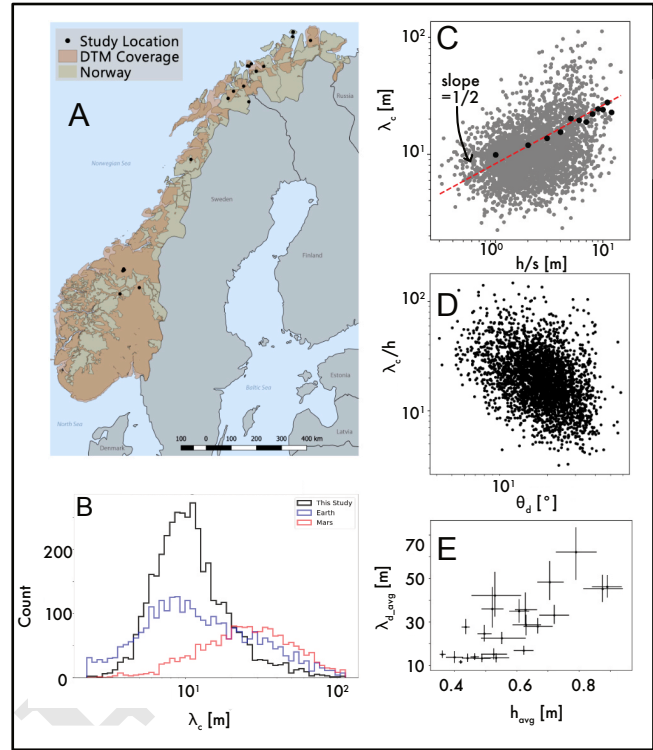


Fig. 3. A) Map of Norway showing study sites used in this paper and DTM coverage. B) Cross-slope wavelength (λ_c) distributions measured in this study, shown with distributions for Earth and Mars from (41). C) Cross-slope wavelength (λ_c) vs. lobe height h /topographic slope s . Red dashed line shows theoretical prediction from Eqn. 6. Black dots show average wavelength split into 13 bins of h/s values. D) Cross-slope wavelength (λ_c) normalized by height h vs. contact angle θ_d at the front of the lobe. E) Downslope terrace wavelength (λ_d) averaged at each site vs. average lobe height for each site.

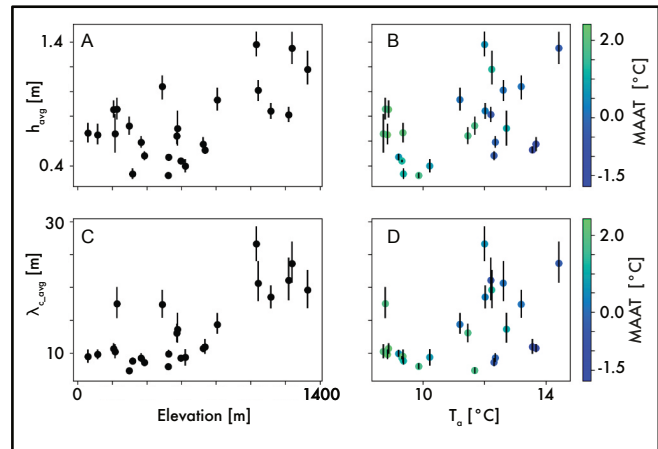


Fig. 4. Relationships between lobe morphology, elevation, and climate indices. Climate data are drawn from daily observations between the years 2000-2020.

Discussion

Our work suggests that even extremely slow-moving soils may exhibit subcritical fluid-like instabilities, but at length and time scales orders of magnitude larger than those observed in thin films. Our new conceptual model for solifluction pattern formation provides a framework for further study. Here we provide some discussion on the most interesting questions resulting from this study, with suggestions for the most promising avenues of exploration.

The initial downslope instability that forms solifluction terraces, which we argue promote the growth of solifluction lobes as a contact line instability, deserves further inspection. While terraces resemble roll waves seen in inertial fluid flows (e.g., (50)), buckling instabilities seen in multilayer flows (51) like rock glaciers (52) and lava flows (53), or wrinkling instabilities found in multilayer solids like pumpkins and human skin (54), our observations of solifluction terrace wavelengths do not fit within these frameworks. Exceedingly slow solifluction velocities exist in a non-inertial regime, which precludes a comparison with roll waves (50). While the positive relationship between downslope wavelength and lobe height is similar to that seen in buckling and wrinkling instabilities, absolute terrace wavelengths can be much larger than lobe height, which is unusual for buckling and wrinkling instabilities; our data show that terrace wavelengths are 1-2 orders of magnitude larger than lobe heights (Figure 2E). Further, the observed low effective viscosities at the surface do not align with buckling instabilities, which typically require a more rigid flow on top (e.g. (52)). However, recent work describes a newly-observed non-inertial instability in shear-thickening flows (e.g., cornstarch mixed with water) that can produce wavelengths much larger than flow thickness (26). These instabilities are shown to result from flow rheology alone, and simply require a rheological curve that exhibits shear-thickening behavior. Our observations of soil velocity profiles, in which effective viscosity increases with depth and therefore shear stress, may align well with a shear-thickening type rheology. Further, our proposed increase in cohesion at soil fronts may also result in an added free surface stabilizing force, which could allow the instability even without shear thickening behavior (26). Further study of these "oobleck waves" may inform the critical conditions necessary for solifluction terrace formation; in turn, field studies of solifluction may provide a natural example of similar instabilities at exceedingly low Reynolds Number, illuminating our understanding of subcritical fluid instabilities.

While we treat solifluction as a non-Newtonian fluid for a first approach, more study is needed to understand the complex rheology of soliflucting soil from a granular perspective. Granular flow rheology is currently understood within the $\mu(I)$ framework, a dimensionless form of the classic shear stress/strain rate relationship that accounts for confining pressure relevant for granular materials (55, 56). In essence, $\mu(I)$ is very similar to fluid rheology, but allows for the role of changing confining pressure with depth. However, the extremely low solifluction velocities observed in the field indicate that solifluction occurs not as a granular flow but well within the granular creep regime (57) that has been shown to describe soil transport velocities on temperate hillslopes (58). Granular creep rheology is still at the forefront of granular physics research. Experiments have shown that creep occurs below the assumed static coefficient of friction (57). While creep rheology is still

uncertain, new models for creep indicate that rather than a viscous-like flow rule, an elastoplastic model may be physically relevant (59). Interestingly, a similar type of model was found to best describe solifluction experiments, rather than a viscous model (60). Experimental and field work is needed to understand whether solifluction is best described as a creeping granular material, a highly viscous non-Newtonian fluid, or some combination of the two, especially given the complex, temporally changing processes (frost heave, gelifluction) that are known to drive it.

Our results also suggest strong connections between climate and solifluction lobe morphology. While much more detailed work is needed to quantitatively understand the role of climate in setting solifluction patterns and lobe morphology, these results suggest that lobe morphology metrics measurable from remote sensing data may contain information about present and past climate, both on Earth and other planets. Additionally, these data show that a changing climate may have substantial effects on solifluction dynamics and morphologies. This relates to a fundamental, yet unanswered question: why do we only see solifluction patterns in cold places? We argue that solifluction provides an example of a contact line instability in a parameter space well outside that of previous studies, with the potential to help shed light on recently observed subcritical fluid instabilities (e.g., (26, 43)) and unstable behavior of soft materials (56). Strong heterogeneity in topography and material properties may be required for the instability to form, as is observed in subcritical fluid fingering over rough substrates (43, 61); it is notable that many arctic hillslopes exhibit solifluction terraces with smooth fronts that are not broken into fingers (8), further supporting the idea that solifluction lobes grow as a secondary instability on top of the downslope instability and require heterogeneity to form. However, we acknowledge that isolated solifluction lobes are also observed in areas with increased soil moisture (8), perhaps behaving similarly to an isolated droplet moving down a plane (62). A better understanding of critical conditions for the onset of the instabilities will also inform our understanding of solifluction lobes seen on Mars, whether they require a cold climate to form, and what explains the larger wavelengths seen on Mars (6, 41). Our findings may also have relevance for earthflows, temperate, slow-moving landslides that exhibit similar morphologic and dynamic characteristics to solifluction lobes (63).

Our analysis is targeted at behavior at the onset of the solifluction lobe instability. Once initiated, the pattern will be self-enhanced as the increased resistance at the raised lobe fronts will further stagger the flow. Nevertheless, more work is needed to understand the evolution of these features through time, as well as possible merging of lobes that would skew measurements toward larger wavelengths. Field studies could examine how disparate lobes interact; for example, once formed, the presence of lobes can redirect water flow through the landscape, influencing lobe development and initiation upslope/downslope (37). For the downslope instability, studies that examine downslope patterns in terrace front exposure dates could determine whether these waves form all at once or initiate at the bottom of a slope and propagate upward. The presence of lobes may also exert a weathering feedback on the underlying bedrock and permafrost, as soil thickness changes substantially along the length of a lobe.

499 Finally, our results highlight the importance of cohesion
500 in landscape evolution. Rather than simply increasing shear
501 strength, as typically assumed in Mohr-Coulomb soil mechan-
502 ics models, we suggest that the presence of cohesion can lead to
503 non-linear dynamics that cause large-scale instabilities in land-
504 scapes. While further field and experimental work is needed
505 to better understand the rheology of arctic soils, we suggest
506 that incorporating formulations of cohesion into soil transport
507 models is key to accurately predict landscape evolution and
508 response to climate change.

509 Materials and Methods

510 **Lobe wavelength data.** Wavelength calculations: Study sites were
511 selected using a combination of high resolution orthophotos and
512 a hillshade of the digital elevation model. We selected 30 hills-
513 slopes on the order of 500 to 1000m long where solifluction was the
514 dominant topographic pattern throughout the domain. Sites with
515 exposed bedrock, gullies, or ponds were avoided. Using a gradient
516 and hillshade map, cross-hillslope groups of solifluction lobes were
517 manually delineated (Figure S1). To streamline and standardize
518 the delineation process, we represent each lobe as a georeferenced
519 triangle. The three vertices defining the triangle were placed along
520 the riser of the lobe at the apex and the two points on either side
521 of the apex where adjacent lobes begin (Figure S1). Lobes were
522 not delineated when riser edges and transitions into adjacent lobes
523 were ambiguous. In addition, some sites contained smaller lobes
524 superimposed on larger terraces or lobes. In these instances we
525 delineated the smaller scale feature. In addition to individual lobes,
526 a minimum of 5 downslope transects were delineated at each study
527 site. Transects were oriented in the direction of the lobes with
528 vertices added each time the transect crossed the riser of a lobe.
529 Over 3500 individual lobes were delineated across 28 hillslopes.

530 For each lobe we used the triangle vector to estimate several
531 planform morphological metrics including lobe orientation, width,
532 and length. To determine orientation we first calculated the line
533 bisecting the interior angle at the apex of the lobe. Lobe orientation
534 was taken to be the direction of this line. Lobe width was calculated
535 as the distance between the two endpoints on either side of the apex.
536 Lobe length was calculated as the minimum distance between the
537 apex and the line connecting the two endpoints. At each lobe a local
538 transect was extracted from the elevation data using a 50m window
539 centered at the lobe apex and in the direction of the bisecting line.
540 Elevation profiles along the transect were extracted using linear
541 interpolation with the number of points in the profile determined by
542 the length of the transect and the DEM resolution (length/cell-size)
543 (figure S1b,c).

544 From the profile, lobe height and contact angle (referred to as
545 riser angle in the solifluction literature) were determined. Transects
546 were first detrended by finding the best fit line to the entire 50m
547 transect in a least squares sense. The slope of the trend line was
548 taken to be the parent slope. To calculate lobe height and contact
549 angle, the detrended profile is subset to only include the portion
550 of the profile representing the manually delineated lobe and 2m
551 down slope of the lobe apex (figure S1d). Height is calculated
552 as the elevation range in the subsetted profile. Contact angle is
553 calculated as the maximum derivative along the subsetted profile
554 using a central differencing scheme (numpy gradient citation).

555 **Climate data.** We use SeNorge2, a gridded meteorological data set
556 with a spatial resolution of 1 square kilometer and a temporal reso-
557 lution of 1 hour to estimate typical climate conditions for each study
558 site. Data comes from the Norway Meteorological Organization and
559 can be found at URL LINK?. While hourly data is available, in
560 this study we used products released at the daily timescale. The
561 variables include maximum daily temperature, minimum daily tem-
562 perature, mean daily temperature, and daily precipitation. The
563 gridded data is interpolated from monitoring stations throughout
564 Norway and is corrected to account for elevation. For full description

of the climate data see (49). We identified each grid cell containing
a study site and extracted the previous 20 years of daily climate
data. We calculated the number of frost cycles per year at each site
where a frost cycle was defined as a zero crossing of the tempera-
ture data. Since the hourly data is summarised at the daily scale
this is equivalent to a change in sign between the maximum daily
temperature and the minimum daily temperature. We used the
surface temperature data as a proxy for ground temperature (i.e.
no corrections/adjustments are made). Justification comes from
experimental studies measuring soil movement due to frost heave
and gelifluction. We averaged the morphology data at each site in
order to compare with the of frost cycles, and bootstrapped 95
confidence intervals for the means.

Data Archival. All data and code used to produce figures will be
available at the NGEE Arctic Data Repository. Norwegian Li-
DAR data are available for download [here](#). Norwegian climate
data are available [here](#). Additional figures and supplementary
information are provided in the SI Appendix.

ACKNOWLEDGMENTS. We would like to thank David Furbish
for substantial help in developing the wavelength scaling analysis;
Bob Anderson, for getting us on the solifluction pattern train in
the first place; Doug Jerolmack, for informative discussions about
granular rheology; Mara Nutt, for help with data collection during
Lobe-a-thon 2020; Charlie Shobe, Anastasia Piliouras, Jon Schwenk,
Yu Zhang, Sajjan Heerah, Cyrano de Bergerac, and Will McDermid
for proof reading and moral support. This project was conducted
under the Next Generation Ecosystem Experiments Arctic (NGEE-
Arctic) project (DOE ERKP757), funded by the Office of Biological
and Environmental Research in the U.S. Department of Energy
Office of Science

1. C Harris, MC Davies, JP Coutard, Rates and processes of periglacial solifluction: an experimental approach. *Earth Surf. Process. Landforms: The J. Br. Geomorphol. Group* **22**, 849–868 (1997).
2. N Matsuoka, Solifluction rates, processes and landforms: a global review. *Earth-Science Rev.* **55**, 107–134 (2001).
3. C Harris, et al., Solifluction processes on permafrost and non-permafrost slopes: results of a large-scale laboratory simulation. *Permafr. Periglac. Process.* **19**, 359–378 (2008).
4. A Johnsson, et al., Arctic landscapes in transition: responses to thawing permafrost. *Eos, Transactions Am. Geophys. Union* **91**, 229–230 (2010).
5. L Kondic, J Diez, Pattern formation in the flow of thin films down an incline: Constant flux configuration. *Phys. Fluids* **13**, 3168–3184 (2001).
6. A Johnsson, et al., Periglacial mass-wasting landforms on mars suggestive of transient liquid water in the recent past: Insights from solifluction lobes on svalbard. *Icarus* **218**, 489–505 (2012).
7. HE Huppert, Flow and instability of a viscous current down a slope. *Nature* **300**, 427–429 (1982).
8. JB Benedict, Downslope soil movement in a colorado alpine region: rates, processes, and climatic significance. *Arct. Alp. Res.* **2**, 165–226 (1970).
9. G Elliott, Microfabric evidence for podzolic soil inversion by solifluction processes. *Earth surface processes landforms* **21**, 467–476 (1996).
10. I Veretennikov, A Indeikina, HC Chang, Front dynamics and fingering of a driven contact line. *J. Fluid Mech.* **373**, 81–110 (1998).
11. S Troian, E Herbolzheimer, S Safran, J Joanny, Fingering instabilities of driven spreading films. *EPL (Europhysics Lett.)* **10**, 25 (1989).
12. RW Style, A Jagota, CY Hui, ER Dufresne, Elastocapillarity: Surface tension and the mechanics of soft solids. *Annu. Rev. Condens. Matter Phys.* **8**, 99–118 (2017).
13. JR Royer, et al., High-speed tracking of rupture and clustering in freely falling granular streams. *Nature* **459**, 1110–1113 (2009).
14. R Brewster, GS Grest, AJ Levine, Effects of cohesion on the surface angle and velocity profiles of granular material in a rotating drum. *Phys. Rev. E* **79**, 011305 (2009).
15. G Prado, Y Amarouchene, H Kellay, Experimental evidence of a rayleigh-plateau instability in free falling granular jets. *Phys. Rev. Lett.* **106**, 198001 (2011).
16. LH Luu, G Castillo, N Mujica, R Soto, Capillarylike fluctuations of a solid-liquid interface in a noncohesive granular system. *Phys. Rev. E* **87**, 040202 (2013).
17. SR Waitukaitis, HF Grütjen, JR Royer, HM Jaeger, Droplet and cluster formation in freely falling granular streams. *Phys. Rev. E* **83**, 051302 (2011).
18. N Mujica, R Soto, Dynamics of noncohesive confined granular media in *Recent Advances in Fluid Dynamics with Environmental Applications.* (Springer), pp. 445–463 (2016).
19. JR de Bruyn, P Habdas, S Kim, Fingering instability of a sheet of yield-stress fluid. *Phys. Rev. E* **66**, 031504 (2002).
20. M Johnson, R Schluter, MJ Miksis, S Bankoff, Experimental study of rivulet formation on an inclined plate by fluorescent imaging. *J. Fluid Mech.* **394**, 339–354 (1999).

637 21. M Spaid, G Homsy, Stability of newtonian and viscoelastic dynamic contact lines. *Phys. Fluids*
638 **8**, 460–478 (1996).

639 22. B Hu, SL Kieweg, Contact line instability of gravity-driven flow of power-law fluids. *J. non-*
640 *Newtonian fluid mechanics* **225**, 62–69 (2015).

641 23. O Voinov, Hydrodynamics of wetting. *Fluid dynamics* **11**, 714–721 (1976).

642 24. JH Kim, HP Kavehpour, JP Rothstein, Dynamic contact angle measurements on superhy-
643 drophobic surfaces. *Phys. Fluids* **27**, 032107 (2015).

644 25. G Seevaratnam, Y Suo, E Ramé, L Walker, S Garoff, Dynamic wetting of shear thinning fluids.
645 *Phys. Fluids* **19**, 012103 (2007).

646 26. BD Texier, H Lhuissier, Y Forterre, B Metzger, Surface-wave instability without inertia in shear-
647 thickening suspensions. *Commun. Phys.* **3**, 1–7 (2020).

648 27. RV Craster, OK Matar, Dynamics and stability of thin liquid films. *Rev. modern physics* **81**,
649 1131 (2009).

650 28. RS Anderson, SP Anderson, *Geomorphology: the mechanics and chemistry of landscapes*.
651 (Cambridge University Press), (2010).

652 29. S Roy, S Luding, T Weinhart, A general (ized) local rheology for wet granular materials. *New*
653 *journal physics* **19**, 043014 (2017).

654 30. SE Yasodian, RK Dutta, L Mathew, T Anima, S Seena, Effect of microorganism on engineer-
655 ing properties of cohesive soils. *Geomech. Eng.* **4**, 135–150 (2012).

656 31. CB Zhang, LH Chen, YP Liu, XD Ji, XP Liu, Triaxial compression test of soil–root composites
657 to evaluate influence of roots on soil shear strength. *Ecol. Eng.* **36**, 19–26 (2010).

658 32. M Pouragha, R Wan, Non-dissipative structural evolutions in granular materials within the
659 small strain range. *Int. J. Solids Struct.* **110**, 94–105 (2017).

660 33. A Seiphoori, Xg Ma, PE Arratia, DJ Jerolmack, Formation of stable aggregates by fluid-
661 assembled solid bridges. *Proc. Natl. Acad. Sci.* **117**, 3375–3381 (2020).

662 34. A Rempel, Formation of ice lenses and frost heave. *J. Geophys. Res. Earth Surf.* **112** (2007).

663 35. N Lu, WJ Likos, Suction stress characteristic curve for unsaturated soil. *J. geotechnical*
664 *geoenvironmental engineering* **132**, 131–142 (2006).

665 36. R Wan, S Khosravani, M Pouragha, Micromechanical analysis of force transport in wet gran-
666 ular soils. *Vadose Zone J.* **13**, 1–12 (2014).

667 37. D Draebing, J Eichel, Spatial controls of turf-banked solifluction lobes and their role for
668 paraglacial adjustment in glacier forelands. *Permaf. Periglac. Process.* **28**, 446–459 (2017).

669 38. J Eichel, et al., Solifluction meets vegetation: the role of biogeomorphic feedbacks for turf-
670 banked solifluction lobe development. *Earth Surf. Process. Landforms* **42**, 1623–1635 (2017).

671 39. N Matsuoka, K Hirakawa, et al., Solifluction resulting from one-sided and two-sided freezing:
672 field data from svalbard. (2000).

673 40. AG Lewkowicz, S Clarke, Late-summer solifluction and active layer depths, fosheim penin-
674 sula, ellesmere island, canada in *Proceedings of the 6th International Conference on Per-*
675 *mafrost. Centre d'études nordiques, Université Laval.* pp. 641–666 (1998).

676 41. R Gastineau, et al., Small-scale lobate hillslope features on mars: A comparative 3d mor-
677 phological study with terrestrial solifluction lobes and zebra stripe lobes. *Icarus* **342**, 113606
678 (2020).

679 42. M Macaulay, P Rognon, Viscosity of cohesive granular flows. *Soft matter* (2020).

680 43. J Marshall, R Ettema, Contact-line instabilities of driven liquid films. *WIT Transactions on*
681 *State-of-the-art Sci. Eng.* **6** (2005).

682 44. N Matsuoka, Climate and material controls on periglacial soil processes: Toward improving
683 periglacial climate indicators. *Quat. Res.* **75**, 356–365 (2011).

684 45. RS Anderson, Near-surface thermal profiles in alpine bedrock: Implications for the frost
685 weathering of rock. *Arct. Alp. Res.* **30**, 362–372 (1998).

686 46. T Hales, JJ Roering, Climatic controls on frost cracking and implications for the evolution of
687 bedrock landscapes. *J. Geophys. Res. Earth Surf.* **112** (2007).

688 47. JA Marshall, et al., Frost for the trees: Did climate increase erosion in unglaciated landscapes
689 during the late pleistocene? *Sci. advances* **1**, e1500715 (2015).

690 48. C Harris, MC Davies, Gelifluction: observations from large-scale laboratory simulations. *Arctic,*
691 *Antarctic, Alp. Res.* **32**, 202–207 (2000).

692 49. C Lussana, et al., senorge2 daily precipitation, an observational gridded dataset over norway
693 from 1957 to the present day. *Earth Syst. Sci. Data* **10**, 235 (2018).

694 50. NJ Balmforth, S Mandre, Dynamics of roll waves. *J. Fluid Mech.* **514**, 1–33 (2004).

695 51. AC Slim, J Teichman, L Mahadevan, Buckling of a thin-layer couette flow. *J. fluid mechanics*
696 **694**, 5 (2012).

697 52. DS Loewenherz, CJ Lawrence, RL Weaver, On the development of transverse ridges on rock
698 glaciers. *J. Glaciol.* **35**, 383–391 (1989).

699 53. RW Griffiths, The dynamics of lava flows. *Annu. Rev. Fluid Mech.* **32**, 477–518 (2000).

700 54. Q Wang, X Zhao, A three-dimensional phase diagram of growth-induced surface instabilities.
701 *Sci. reports* **5**, 1–10 (2015).

702 55. P Jop, Y Forterre, O Pouliquen, A constitutive law for dense granular flows. *Nature* **441**,
703 727–730 (2006).

704 56. DJ Jerolmack, KE Daniels, Viewing earth's surface as a soft-matter landscape. *Nat. Rev.*
705 *Phys.*, 1–15 (2019).

706 57. M Houssais, CP Ortiz, DJ Durian, DJ Jerolmack, Onset of sediment transport is a continuous
707 transition driven by fluid shear and granular creep. *Nat. communications* **6**, 1–8 (2015).

708 58. B Ferdowsi, CP Ortiz, DJ Jerolmack, Glassy dynamics of landscape evolution. *Proc. Natl.*
709 *Acad. Sci.* **115**, 4827–4832 (2018).

710 59. A Nicolas, EE Ferrero, K Martens, JL Barrat, Deformation and flow of amorphous solids:
711 Insights from elastoplastic models. *Rev. Mod. Phys.* **90**, 045006 (2018).

712 60. C Harris, MC Davies, BR Rea, Gelifluction: viscous flow or plastic creep? *Earth Surf. Process.*
713 *Landforms: The J. Br. Geomorphol. Res. Group* **28**, 1289–1301 (2003).

714 61. J Marshall, S Wang, Contact-line fingering and rivulet formation in the presence of surface
715 contamination. *Comput. & fluids* **34**, 664–683 (2005).

716 62. L Mahadevan, Y Pomeau, Rolling droplets. *Phys. fluids* **11**, 2449–2453 (1999).

717 63. P Lacroix, AL Handwerger, G Bièvre, Life and death of slow-moving landslides. *Nat. Rev.*
718 *Earth & Environ.* **1**, 404–419 (2020).